

The Large Magellanic Cloud globular cluster NGC 1866: new data, new models, new analysis¹

Vincenzo Testa

Osservatorio Astronomico di Roma

Via Frascati, 33 00040 Monteporzio Catone, Italy

`testa@oar.mporzio.astro.it`

Francesco R. Ferraro¹

European Southern Observatory

Karl Schwarzschild Strasse 2, D-85748 Garching bei München, Germany

Alessandro Chieffi

Istituto di Astrofisica Spaziale, C.N.R.

Via del Fosso del Cavaliere, 00100 Roma, Italy

Oscar Straniero

Osservatorio Astronomico di Collurania

Via Maggini, 88 64100 Teramo, Italy

Marco Limongi

Osservatorio Astronomico di Roma

Via Frascati, 33 00040 Monteporzio Catone, Italy

and

Flavio Fusi Pecci¹

Stazione Astronomica di Cagliari

09012 Capoterra, Italy

ABSTRACT

¹On leave from Osservatorio Astronomico di Bologna, via Ranzani 1, I-40126 Bologna, ITALY

We present a new deep (down to $V \sim 24$) photometry of a wide region ($\sim 6' \times 6'$) around the LMC globular cluster NGC1866: our sample is much larger (by more than a factor three) than any previous photometry and with a main sequence which may be considered complete, down to at least 3 mag below the brightest MS star: such an occurrence allows a meaningful and robust comparison with various theoretical scenarios produced by means of models computed with the evolutionary code FRANEC. Both age and present mass function slope, α , are derived by a fit to the available MS and by the use of the parameter $\Delta\sigma$, which is simply the difference, in σ 's, between the observed and predicted integrated MS luminosity functions. Our main conclusions are:

a) the adoption of standard models (i.e. computed by adopting the Schwarzschild criterion to fix the border of the convective core) allows a fair fit to the MS for an age of the order of 100-140 Myr and a present mass function having a slope α between 2.3 and 1.9, the exact values depending on the adopted distance modulus. It is moreover possible to reproduce the average He clump luminosity while the total number of stars predicted in the He clump is twice the observed value: this means that we re-obtain and confirm the first finding of Becker and Mathews (1983), according to whom the simple adoption of a "classical" scenario leads to a neat discrepancy concerning the prediction of the number of stars in the He clump.

b) the adoption of models computed by increasing the size of the convective core by a certain amount, i.e. $0.25 H_p$, leads to a fair fit to the main sequence only for a visual distance modulus $(m - M)_V \simeq 18.6$, an age $t \simeq 200 \text{ Myr}$ and $\alpha \simeq 2.2$. In this case, the total number of He clump stars is well reproduced, although the luminosity function of the He clump itself is predicted to be systematically less luminous than observed.

The previous conclusions are based on the assumption that there is no appreciable population of binaries in NGC 1866. Though there are not yet sufficient data on the frequency of binary systems in these clusters, we analyzed how the previous scenarios would change if a consistent ($\simeq 30\%$) population of binary systems were present in the cluster. This choice is based on the fact that a fraction of binaries of the order of 30% has already been found in NGC 1818, a cluster similar to NGC 1866 (Elson et al. 1998). The inclusion of a 30% binary population leads to the following conclusions:

c) the adoption of the standard models now leads to a good fit to the entire luminosity function, i.e. main sequence, turn off, and He clump stars, for a visual distance modulus $(m - M)_V = 18.8$, an age $t \simeq 100 \text{ Myr}$ and a mass function slope $\alpha \simeq 2.4$, thus largely removing the "classical" discrepancy between observed and predicted number of stars in the He burning clump. The quoted visual distance modulus constrains the unreddened distance modulus $(m - M)_0$ within 18.50 and 18.62, depending on the reddening (whose most common values available in the literature range from 0.05 to 0.10).

d) at variance with point c), the fit obtained by using models computed with an enlarged convective core gets worse when a binary component is taken into account. This is due to the fact that the presence of binary systems increases the existing discrepancy between the observed and predicted clump luminosity, since the He clump is predicted to be even less luminous than in absence of binaries.

As a consequence of this analysis, we think that the next step towards a proper understanding of NGC 1866, and similar clusters, must include the accurate determination of the frequency of binary systems that will be hopefully performed with the incoming Cycle 8 HST observations of NGC 1866.

Subject headings: galaxies: star clusters, Magellanic Clouds, color-magnitude diagrams

1. Introduction

NGC 1866 is one of the most largely studied stellar clusters in the Large Magellanic Cloud (LMC). Since the first photometric study by Arp and Thackeray (1967), who discovered a large number of member Cepheid variables, this cluster has been recognized as an ideal laboratory for testing stellar evolutionary models of intermediate-mass stars. NGC 1866 is one of the most populous LMC clusters, having a mass comparable to that of a typical globular cluster in the Galaxy

¹Based on observations obtained at ESO, La Silla, Chile

($M = 1.25 \pm 0.25 \times 10^5 M_\odot$ Fischer et al. 1992) and is relatively young to study the evolution of intermediate-mass ($M \sim 5M_\odot$) stars. These stars develop a convective core during the H-burning phase and represent the ideal target for an analysis of the real extension of the convective cores, i.e., to see whether the size of convective cores, as determined by the Schwarzschild criterion, to which we will refer as “standard”, must be “artificially” increased in order to fit the observational data. This is a long-standing problem whose solution would deeply influence many aspects of our present understanding of the universe: in fact it would fix a key parameter in the computation of the stellar evolution which would reflect, e.g., on the intermediate age clusters, on the determination of the various mass limits, like m_{up} and m'_{up} (see Castellani et al. 1971; Becker and Iben 1979; Castellani et al. 1985) and on the initial-final mass relation, on the relation between He-core mass and initial mass for massive stars that is linked to the problem of metal enrichment.

NGC 1866 has often been considered a “proof” for the existence of the convective overshooting (Becker and Mathews 1983; Chiosi et al. 1989). Actually the fit to this (or another) cluster can only give us information on the likely size of the convective core but it ascertains the mechanism which determines the size. For reasons sinking in the history of the computation of stellar models in the range of massive stars (whose analysis goes well beyond the purposes of this paper), this problem has always been (unfortunately!), interpreted in terms of “overshooting”, therefore as a proof of the existence or non-existence of a specific phenomenon where the convective cells cross the classical border of the convective core and mix more matter than predicted in the “classical” scenario, thus producing a larger amount of fuel. This direct connection is meaningless: in fact, if the observations showed that the convective core must be larger than currently predicted by the models, various causes could be considered. Just to mention two possibilities other than the “overshooting”, the simple change from the old Cox-Tabor opacities (Cox and Tabor 1976) to the Los Alamos ones (Huebner et al. 1977), which occurred at the beginning of the 80’s, led, by itself, to a significant increase of the classical size of the convective core. A second possibility, proposed for example by A. Maeder (private communication) is a rotationally induced mixing that leads to a more massive convective core.

Becker and Mathews (1983) were the first to point out that the “standard” models could not fit the observed ratio of main sequence vs He clump stars (N_{MS}/N_{He}): they found that their standard models predicted at least 4 times more giant stars than observed with respect to the main sequence ones. In the following years, Chiosi et al. (1989, hereafter C89) and Brocato et al. (1989, hereafter B89), studied in detail the properties of the stellar content of NGC 1866, using CCD data. A detailed discussion of the general problem as well as the results of C89 and B89 are given in Wood (1991). Briefly, B89 concluded that the standard models reproduce both the color-magnitude diagram (CMD) morphology and the luminosity function (LF) of the cluster, while C89 concluded that models including a certain amount of overshooting were required.

The problem has been further discussed in later papers (Lattanzio et al. 1991; Brocato et al. 1994, hereafter BCP94) without reaching an agreement. A larger sample of data led BCP94 to conclude that their previous set of data was substantially correct, whereas the ones adopted by

C89 were affected by stochastic fluctuations. Actually, the sample adopted by C89 included 554 MS stars (down to $V = 19.2$) and 41 He burning giants, while the latest set of data presented by BCP94 included (down to the same magnitude) 462 MS stars and 65 giants. All these numbers were already corrected by the authors for completeness, crowding and field stars contamination.

In order to contribute to clear up the situation, we began a project specifically devoted to a complete photometric study of the stellar population in NGC 1866, including a substantial part of the MS. In this paper, we present a new deep (down to $V \sim 24$) photometry of a wide region $\sim 6' \times 6'$ around the cluster.

The observations and reduction procedures are described in sect. 2, while the morphology of the inferred CMD is presented and discussed in sect. 3. Sect. 4 is devoted to the discussion of the derived LF, with a special attention to the field decontamination and the completeness estimate and correction, together with the comparison with previous studies. The comparison with various theoretical scenarios is discussed in sect. 5. A final section with summary and conclusions follows.

2. Observations, Reductions and Calibrations

2.1. Observations and Reductions

The data have been obtained at the 2.2m ESO-MPI telescope at La Silla (Chile), on Jan. 27th, 1993. We used EFOSC2 equipped with the CCD #19 Thomson of size 1024×1024 pixels, with a scale of $0.363''/\text{pix}$, which yields a total field of view of $\sim 6' \times 6'$. During the night we secured B,V frames in two fields around NGC 1866: *FA*, roughly centered on the cluster center and *FB*, located at $\sim 6'$ SE from the cluster center and observed for statistical field decontamination purposes.

Figure 1 shows a computer map of the two fields. A circle is drawn at $\sim 6'$ from the cluster center and encloses the region dominated by stars belonging to the cluster. According to Bertelli et al. (1992), at larger distances the contribution of the cluster stars to the total population of the field is expected to drop below 1%. The average observational conditions were good, and the seeing was around $1''$. A journal of the observations is reported in Table 1.

The reductions were performed using DAOPHOT (Stetson 1987), implemented on IRAF³. In order to identify stars within each frame, we followed the standard procedure as described on the DAOPHOT manuals, and used the routine ALLSTAR to perform the final PSF-fit.

Each frame was reduced independently, then a frame in each filter has been chosen as *reference* frame for coordinate and magnitude transformations (reference frames are marked with an asterisk in Table 1); then all the frames have been transformed to the reference system in order to get a homogeneous set of instrumental magnitudes and coordinates.

³IRAF is operated by AURA, Inc., under cooperative agreement with the National Science Foundation

Table 1. Observed Frames

Image	filter	exp. time
FA0122*	V	30 <i>s</i>
FA0124	B	60 <i>s</i>
FA0125	B	60 <i>s</i>
FA0127	V	15 <i>s</i>
FA0128	V	15 <i>s</i>
FA0130	B	60 <i>s</i>
FA0131	V	5 <i>s</i>
FA0133	B	15 <i>s</i>
FA0134	V	480 <i>s</i>
FA0136	B	120 <i>s</i>
FA0139	B	1500 <i>s</i>
FB0140	V	30 <i>s</i>
FB0142	B	90 <i>s</i>
FB0143	B	1500 <i>s</i>
FB0144*	V	480 <i>s</i>

A set of averaged instrumental magnitudes (weighed according to the photometric quality of the frames) have then been obtained for each field. The overlap region between the two adjacent fields has been used to transform the coordinates into a common local system. In this arbitrary system, the center of the cluster has been estimated at pixel (520,520) in *FA* (see Figure 1).

2.2. Calibrations

Since the observations were performed during slightly non-photometric conditions, we used the well-calibrated photometric sequence of standard stars obtained by Walker (1995) in the surrounding region of NGC 1866, to link the instrumental magnitudes to the standard Johnson system. The cross-correlation between our data set and Walker’s own identified 2294 stars in common, which were used to calibrate the final catalog.

The list of the final calibrated B,V magnitudes and position for 12680 (*FA*) + 3044 (*FB*) stars identified in our survey is available in electronic form. Table 2 reports a sample of the table of photometry of *FA* while Table 3 reports the analogous for *FB*. Figure 2a shows the CMD for stars in *FA* (hereafter referred to as CLUSTER sample); in the same way, Figure 2b shows the CMD for stars lying at $r > 6'$ from the cluster center, which are assumed to be representative of the field population around the cluster (hereafter referred to as FIELD sample).

3. The Color-Magnitude Diagram

3.1. Overall Morphology

The analysis of the CMDs, presented in Figure 2a and Figure 2b for the CLUSTER and the FIELD sample respectively, shows that the overall morphology of the main stellar populations in the NGC 1866 region is well-defined. In particular, in Figure 2b, some typical features of the population mix in the field are evidenced (see also the discussion by Walker 1995; Bertelli et al. 1992):

(i) the field multi-population main sequence (MS) extending up to $V \sim 16$ merges into the MS of NGC 1866

(ii) a pretty well-defined giant branch of a presumably old (some Gyr, see Walker 1995) stellar population is clearly visible at $(B - V) > 0.7$ and $V < 21$.

(iii) a red giant clump is located at $V \sim 19$, indicating the existence of an intermediate-age population having $t > 500$ Myr, (see Brocato et al. 1989; Walker 1995)

On the other hand, from the comparison of Figure 2a and Figure 2b the main features of the cluster population are also visible:

Table 2. Photometry of CLUSTER frame

Id.num.	X	Y	V	$\sigma(V)$	$B - V$	$\sigma(B - V)$
1	170.77	0.86	19.68	0.01	0.01	0.03
2	859.86	1.49	20.31	0.02	0.09	0.03
3	867.64	8.95	22.23	0.07	0.45	0.10
4	528.30	1.72	18.91	0.01	-0.05	0.01
5	466.28	1.87	22.48	0.07	0.61	0.09
6	611.78	2.28	22.78	0.09	0.32	0.13
7	57.47	2.49	21.58	0.04	0.47	0.07
8	479.96	2.62	20.72	0.01	0.10	0.02
9	942.88	2.92	22.65	0.09	0.95	0.16
10	851.31	3.07	21.45	0.05	0.24	0.06
11	368.49	3.28	22.90	0.10	0.11	0.13
12	129.26	8.74	21.33	0.02	0.21	0.04
13	25.95	3.77	22.36	0.09	0.54	0.12
14	295.52	5.51	21.49	0.03	0.35	0.04
15	444.89	5.91	19.03	0.00	-0.07	0.01
16	104.19	5.99	22.64	0.09	0.48	0.13
17	224.52	6.15	22.27	0.04	0.47	0.08
18	319.41	11.00	22.39	0.06	0.54	0.09
19	180.74	6.75	23.20	0.13	0.73	0.20
20	383.21	9.18	21.94	0.03	0.32	0.05

Table 3. Photometry of FIELD frame

Id.num.	X	Y	V	$\sigma(V)$	$B - V$	$\sigma(B - V)$
1	58.44	1.00	19.71	0.02	0.66	0.07
2	175.82	1.20	22.03	0.04	0.33	0.11
3	572.97	1.74	21.06	0.04	0.22	0.05
4	5.74	1.65	22.75	0.16	1.59	0.50
5	544.28	4.60	21.57	0.03	0.23	0.05
6	444.44	2.68	21.75	0.04	0.27	0.05
7	457.46	2.71	21.20	0.01	0.34	0.03
8	366.48	4.05	21.56	0.03	0.53	0.05
9	747.11	5.92	21.79	0.05	0.34	0.07
10	109.36	4.62	21.38	0.02	0.19	0.04
11	990.28	12.23	21.20	0.06	0.11	0.11
12	333.27	5.92	21.19	0.02	0.28	0.03
13	203.43	5.92	20.47	0.02	0.35	0.03
14	561.95	5.95	22.53	0.06	0.30	0.09
15	401.76	6.94	21.36	0.04	0.30	0.05
16	400.46	12.52	19.40	0.01	0.08	0.02
17	397.26	17.49	20.58	0.01	0.48	0.02
18	78.37	6.96	20.66	0.01	0.06	0.02
19	677.36	7.24	21.40	0.02	0.32	0.03
20	532.09	7.86	20.43	0.01	0.83	0.02

(iv) the bright He-burning clump between $V \sim 15.5$ and $V \sim 16.5$ ($B - V \sim 0.5$ and $B - V \sim 1.0$)

(v) a fairly well-populated AGB which extends up to $V \sim 15$ and $(B - V) \sim 1.5$. In addition, some stars lying in the portion of CMD, that we assume populated by the field, belong to the cluster and are late AGB stars detected and studied in the near-IR (Frogel et al. 1990). We shall discuss this point later on.

These features have no correspondence in the FIELD sample. On the basis of these considerations, we can define three main regions in the CMD:

- (1) the cluster Red Giants (CLUSTER RGs) for $(B - V) > 0.4$ and $V < 17$
- (2) the field Red Giants (FIELD RGs) for $(B - V) > 0.5$ and $V < 21$
- (3) the cluster Main Sequence (CLUSTER MS) for $(B - V) < 0.5$.

All these regions are separated by dashed lines in Figure 3.

However, in order to better enucleate the main features of the cluster population with respect to the field ones, we divided the CLUSTER sample in 5 concentric annuli:

- annulus 1: $r < 29''$ ($80pix$);
- annulus 2: $29'' < r < 45.4''$ ($80 - 125pix$);
- annulus 3: $45.4'' < r < 90.7''$ ($125 - 250pix$);
- annulus 4: $90.7'' < r < 130.7''$ ($250 - 360pix$);
- annulus 5: $130.7'' < r < 181''$ ($360 - 500pix$);

Figure 4(a-f) shows the radial CMDs for the five annuli defined above (panels a to e) compared with the FIELD sample (panel f). As we can see, although conspicuous errors affect the photometry in this crowded region, the innermost annulus (annulus 1) is clearly dominated by the cluster population: no features of the field populations are present in this CMD, while both the CLUSTER RGs clump and the AGB are clearly visible. On the other hand, the FIELD RGs regions become, as expected, more and more populated at growing distances from the cluster center (annuli 2, 3, 4, 5), and the main features of this population (the red clump and the old red giant branch) progressively become more and more evident (compare panel (c),(d),(e), with panel (f) in Figure 4). Another feature, which can be easily evaluated from Figure 4 (panels (a), (b), (c)) is the termination point of the cluster MS which is fairly well defined and turns to be located at $V = 16.8 \pm 0.1$.

3.2. Photometric errors

In order to estimate photometric errors, we considered the internal errors from DAOPHOT combined with the uncertainty of the calibration procedure and, when possible, frame to frame scatter (i.e. for the shallow frames). We report in Figure 5(a-l) the mean photometric errors in V and $(B-V)$ for each of the five annuli defined above, averaged over 0.5 mag-wide bins. As expected, larger errors occur in the most internal crowded regions (annulus 1) and at fainter magnitudes.

3.3. The completeness

Since one of the main goals of this paper is to present meaningful LF and population ratios, the treatment of the completeness of the observed sample is a crucial problem: for this reason, we shall discuss this point in detail.

The problem of estimating the completeness factor for a stellar population comes out dramatically when increasing the crowding conditions of the observed field. On the other hand, the crowding conditions depend, to a zero-th order, on the distance from the cluster center: in the second place, on the seeing because in bad seeing conditions, it is more likely to blend close stellar images. The final effect of this phenomenon is the loss of fainter stars and, eventually, the appearances of spurious bright objects, that could remarkably alter the resulting LF.

In order to (quantitatively) estimate the fraction of objects lost in each magnitude bin, λ_c , we carried out extensive *artificial star tests*. This procedure has been described in detail in many papers (e.g. Mateo 1988; Bolte 1989; Sandquist et al. 1996). The basic idea is to add a number of “artificial stars” (i.e. objects having the same characteristics of the *real* stars in the frame) to the original frame, and to reduce once again the new *enriched* frame. In the specific case of NGC 1866 (as in the case of any LMC cluster), the fact that the cluster is almost completely contained within a single frame generates a large density gradient within the frame and requires that the completeness parameter be evaluated also as a function of the distance from the cluster center. For this reason, we adopted the sub-division in concentric annuli defined in Section 3.1 to quantify the dependence of the incompleteness on the distance from the cluster center (i.e. on the crowding conditions). For each annulus we generated a set of *artificial* stars for each bin of magnitude (0.5 mag wide) over the entire magnitude range covered by our observations ($V \sim 15 - 24$). In order to avoid spurious crowding enhancement due to the enrichment procedure, only 20-30 stars were added to the original frame in each iteration, and the procedure was then repeated many times. A virtually identical reduction procedure was performed on the *enriched* frames in order to ensure a homogeneous treatment of both artificial and original frames. The output list of stars (reporting magnitude and positions) was then cross-checked with the list of artificial stars added to the frame. Each artificial star was considered “*detected*” if the following criteria were satisfied: $\Delta X < 2pix$, $\Delta Y < 2pix$, $\Delta mag < 0.3$, where ΔX , ΔY and Δmag are the differences in position and magnitude of the recovered star with respect to the simulated one.

The completeness factor (λ_c) in each annulus (where the crowding density can be considered constant) and in each bin of magnitude was finally derived by the ratio between the number of artificial stars recovered (N_{rec}) and the number of stars originally simulated (N_{sim}): $\lambda_c = N_{rec}/N_{sim}$.

The procedure was applied independently to the deepest images in both filters and repeated many times: a total of more than 10,000 artificial stars have been simulated. According to Mateo (1988), the final completeness factor (Λ) to each point ($V, B - V$) of the CMD is $\Lambda = \lambda_c^V \times \lambda_c^B$. Following this procedure, the completeness level at the CLUSTER RGs region is $\sim 100\%$ in both the filters, while the correction factor in the five considered annuli for the CLUSTER MS are plotted in Figure 6. The completeness of our sample is high ($> 80\%$) down to $V \div B < 22.5$ in the most external regions (annuli 3,4,5), then start to significantly decrease in annulus 2 (being $> 60\%$ down to $V \div B < 21$), and drops rapidly down to 40% in the central field (annulus 1), even at a relatively bright magnitude level ($V \div B \sim 19$). For this reason, we decide to exclude the contribution of this very central region (annulus 1) in deriving the LF.

3.4. Field Subtraction

The traditional zapping technique consists in gridding the two CMDs, “cluster+field” and “field”, and count the stars in each cell in the two diagrams after normalizing the areas and correcting for completeness. Then, an equivalent number of stars is removed from the single cells of the diagram of “cluster+field”, on the basis of the number of field stars found in the diagram of the “field” alone. This technique has two major problems:

- the *a priori* gridding leads to the possibility that populous sequences are arbitrary cut by the cell boundaries, and one cell is more affected than others by the subtraction. In this way spurious sequences could be generated, as for example in the case of an almost vertical MS cut in half by the cell boundaries, with a slightly redder field population MS;
- if, within a single cell, the stars to be dragged out are chosen at random from the sample, clearly the probability of picking stars where the density is higher, i.e. in the vicinity of the sequence, is large. The result would be an artificial depletion of populous sequences. A possible solution is to trace a mean ridge line, and attribute weights to the points so that it is more likely to drag out stars lying far from the sequence rather than close to it.

In order to avoid these problems, in the following we adopted the method described by Mighell et al. (1996). This method considers, for each star in the “cluster+field” CMD, its own cell, then counts the stars which fall in the cell, in the two diagrams (“cluster+field” and “field”, respectively).

The size of the cells are determined on the basis of the error-box associated to each star, i.e. $[\pm MAX(2\sigma_V, 0.200), \pm MAX(2\sigma_{B-V}, 0.100)]$. A probability is then assigned to each star:

$$p = 1 - MIN\left(\frac{\alpha(N_{FIELD} + 1)}{N_{CLUSTER} + 1}, 1.0\right)$$

where α is the ratio of the areas of the field and of the cluster, N_{FIELD} and $N_{CLUSTER}$ are the number of stars corrected for completeness in each cell of the “field” and in the “cluster+field” CMDs, respectively. Then, a random number p' is extracted, between 0 and 1. If $p' < p$, the star is taken, otherwise is discarded.

As already quoted in Section 2.1, in this paper we assumed as FIELD sample all the observed stars lying at $r > 6'$ from the cluster center. This area measures $\sim 16.8'\square$.

3.5. Comparison with published results

As we said beforehand, in the literature there are at least three previous photometric surveys specifically aimed at studying the stellar population in NGC 1866: C89, B89 and the revision by BCP94. In these papers, the authors presented LFs based on independent photometric studies of the cluster: the region sampled in each of the three papers are all included in the field covered by our observations. Moreover, the CMD plotted in Figure 2 and Figure 3 is by far the deepest, most accurate and populous CMD ever published for NGC 1866 (compare our Figure 3 with Figure 5 in B89 and Figure 7 in C89 or even Figure 2 in BCP94). For this reason we will use our sample in order to establish the existence of any systematic difference, bias or incompleteness which may affect the previously published samples.

Magnitudes and positions of the stars for all the published samples have been kindly provided by the authors in electronic form.

3.5.1. Comparison with C89

The field observed by C89 covers an area of $\sim 2' \times 3'$ roughly centered on the cluster center (see Figure 1 by C89). Their pixel size is comparable to ours ($0.363''/\text{pix}$).

First of all, the sample observed by C89 has been reported in our coordinate system. The cluster center assumed by C89 is located at $(X_{C89} = 507.82, Y_{C89} = 515.42)$, slightly different from the one assumed in our sample. However, in order to be fully consistent with the assumption of C89 we adopted, in the comparison, the above coordinates for the cluster center.

Then, we searched for any systematic difference in magnitudes and colors between the two samples over the whole region in common in our field and C89. The stars in common between the two catalogs have been used to derive the equations relating C89 magnitudes to our system. The equations are reported below:

$$V = V_{C89} + 0.145 + 0.014(B - V)_{C89}$$

$$B - V = (B - V)_{C89} + 0.014.$$

Once the magnitudes and the position of the original C89 list were reported to our system, we performed an accurate search for the stars in common in the specific area selected by C89 to construct the *normalized* LF. The field specifically considered by C89 in their analysis is located between $r_{int} = 85pix$ and $r_{out} = 160pix$. This area ($\sim 2.4'\square$) is represented as a horizontally striped region labeled 'C89' in Figure 7. Stars have been considered identified under the following assumptions

$$\Delta X < 2pix, \Delta Y < 2pix, \Delta mag < 0.3$$

Figure 8 summarizes the results of the comparison: in particular, in Figure 8 we plotted the CMD for the 652 stars found in common in the selected area (panel a), stars which have been found ONLY in our sample (panel b), and stars which have been measured only in the C89 sample (panel c).

According to C89, dashed lines delimit different regions of the CMD mainly dominated by different populations (see their figure 7). In particular, (a) the region dominated by the cluster Main Sequence (MS) at $(B - V) < 0.5$, (b) the FIELD RGs at $(B - V) > 0.5$ and $V > 17$, and (c) the CLUSTER RGs stars at $(B - V) > 0.5$ and $V < 17$. Moreover, the CLUSTER RGs region has been divided into three sub-groups (labeled A,B,C) as suggested by C89. It is worth noting that while C89, at first, suggested to use only giants counted in Group A and B (since “*group C likely do not belong to the same population as those of group A and B*”), they later adopted (in normalizing the MS LF) always the whole CLUSTER RGs population (group A+B+C) (see their Table 1 and the further discussion in their Sect. 4).

The most relevant results of the comparison are:

- (i) Only 4 stars (over 656 stars) have no counterpart in our catalog (two of them are in the region of the CMD dominated by the field population – see Figure 8c)
- (ii) The C89 list turns out to be seriously incomplete with respect to our sample, even at relatively bright magnitudes ($V > 18$);
- (iii) All the 39 bright RGs (BRG) stars found by C89 have been identified in our sample. In addition, we found another BRG (namely star 3023: $V = 16.5$ and $B - V = 1.0$) which has no counterpart in the C89 catalog (see Figure 8b).
- (iv) A BRG (namely 1018 in the C89 catalog) looks like a blend of two stars: one of the two blended components still lies, though at a fainter magnitude, in the BRGs region (Sector B - See Figure 8b); therefore this fact does not affect the total number of BRGs.

3.5.2. Comparison with B89

B89 sampled 4 fields ($4' \times 2'.5$ each) at different distances from the cluster center. One of the fields was centered on the cluster and was used by the authors to construct the LF. We checked the relative photometric calibration with respect to B89, following the same procedure described above (with the same assumptions).

After applying the cross-correlation procedure, 1355 stars in common have been found and have been used to obtain the following equations which relate the B89 magnitudes to our system:

$$V = V_{B89} - 0.05 - 0.12(B - V)_{B89} + 0.11(B - V)_{B89}^2$$

$$B = B_{B89} + 0.02 - 0.38(B - V)_{B89} + 0.31(B - V)_{B89}^2$$

In this case, we adopted a second order polynomial to derive the correction. This gives a smoother relation that takes into account both the small corrections at bright magnitudes and bluer colors and the larger correction at faint magnitudes and redder colors. However, the overall corrections are in general very small ($\Delta mag < 0.1$). The region selected by B89 for constructing the LF is an annular region ranging $47'' < r < 134''$ from the center. This area ($\sim 9.3' \square$) is indicated as a tilted, diagonal shaded region, labeled as 'B89', in Figure 7.

Similarly to Figure 8, Figure 9 reports the CMDs resulting from the comparison between our catalog and B89, in the region selected by B89 for constructing the LF.

In this case too, the main results of the comparison closely resemble the discussion reported in the previous section. In summary:

(i) All the 52 BRGs found by B89 have been identified in our sample, and as previously found in the comparison with C89 an additional BRG has been identified in our sample (namely star id. 1018);

(ii) also in this case the B89 sample appears to be seriously incomplete for $V > 18.5$.

Interestingly enough, B89 did not perform any statistical decontamination from field stars in the region of the CLUSTER RGs and in normalizing the MS LF they used all the 52 RGs identified.

3.5.3. Comparison with BCP94

BCP94 completed the B89 survey presenting a (V,V-R)-CMD for an extended region around the cluster (see Figure 1 in BCP94). As in the previous comparisons, we used their sample in order to find systematic difference in magnitudes and/or colors. In this specific case, only the V

magnitudes could be compared to our photometry. The BCP94 V magnitudes match our system by applying only a small offset:

$$V = V_{BCP94} - 0.05$$

A detailed analysis of the stars in common has been carried out only in the region that the authors chose for constructing the LF. This area is the annulus limited by the largest dashed circle which complete the area surveyed by B89 and labeled as 'BCP94' in Figure 7. The extension of the region discussed by BCP94 is $\sim 13.8' \square$. Figure 10 presents the CMDs obtained from this comparison. As can be seen, the limiting magnitude of the BCP94 sample is located at $V \sim 19$. It is interesting to note, however, that in this case, for $V < 19$, only few stars in the cluster MS region are present in our list and are missing from the BCP94 list. In particular, all the 65 BRGs found by BCP94 have been identified. Figure 11 shows the comparison of the integrated stars counts between the sample presented here and the three previous samples (C89, B89, BCP94, respectively). All stars lying in the sector of the CMD defined as MS in Figure 3, in each of the regions selected by the various authors have been used for this comparison. No corrections (neither for completeness nor for field contamination) have been applied to the star counts.

The ratio of the stars counted in each magnitude bin can be used to derive the “*relative*” completeness ratio of each sample with respect to ours. The comparison shows that the completeness ratio decreases to less than $\sim 50\%$ at $V \sim 19.3$ for C89 and BCP94 and at $V \sim 20$ for B89, respectively.

4. Results

4.1. The CLUSTER CMD: decontaminating the observed sample

The decontamination procedure described in Section 3.4 has been applied to each of the 5 radial annuli defined in Section 3.1. The procedure has been applied only for magnitudes brighter than $B \div V = 22$, because the LF will be studied only down to the magnitude bin where the overall completeness drops below 50%, to prevent problems due to statistical fluctuations close to the cutoff line. Moreover, field decontamination at faint magnitudes requires too high completeness corrections, which could give rise to unreliable star counts.

Figure 12 reports the CMDs in the radial annuli 1, 2, 3, 4 and 5 before and after the field decontamination, respectively. As discussed in Section 3.3, the innermost region (annulus 1) will not be used in the construction of the LF and for this reason it will not be considered in the following discussion. Thus, the final adopted sample covers the region in the FA field over a radial range $29'' < r < 180''$ (annuli 2+3+4+5). This field has approximately an extension of $\sim 37.6' \square$.

A particular attention has been given to the statistical decontamination of the region dominated

by the CLUSTER RGs, since this population is used to normalize the MS LF in the comparison with the previous works, and -this is even more important- it is the test population that will be considered in the following model comparison. Seven stars in the FIELD sample have been found to lie in the region of the CMD labeled as CLUSTER RGs, thus we expected ~ 16 field stars lying in that area of the CMD. This leads to a final number of 107 RGs after the statistical decontamination from the field stars that will be considered in the following discussion. Figure 13 reports the final decontaminated CMD for the global adopted sample (obtained co-adding the CMDs of annuli 2, 3, 4, and 5). The dashed lines reported in Figure 13 identify the regions defined in Figure 3. There are few stars beyond the red limit of the CLUSTER RGs box, which are indicated as Late-AGB stars. These have been identified from the near-IR sample of Frogel et al. (1990) as stars in the thermally pulsing AGB phase. Since our models do not include the latest stages of AGB evolution, and this evolutionary phase is very short within the lifetime of a star, we will not consider them in the giant sample in the following analysis and discussion.

4.2. The MS stars Luminosity Function

In order to obtain the Luminosity Function of the CLUSTER MS stars, we followed a standard procedure already used in other papers (see, e.g., Ferraro et al. 1997). First, we determined the mean ridge line (MRL) of the MS was from the statistically decontaminated sample plotted in Figure 13, by adopting an iterative procedure: the sample was divided into 0.2 mag-wide bins, then, for each bin, the star distribution in $(B - V)$ color was computed, the mode of the distribution was assumed as first-guess equivalent color, and all the objects lying more than $\pm 7\sigma$ away from the mode were rejected. Secondly, the mode of distribution was re-computed until convergence. When constructing the LF, only stars lying, in each 0.2 mag-width bin, within $\pm 7\sigma_{B-V}$ from the MRL were counted. However, since the sequence’s width depends on the errors, we performed the star selection for the LF in each annulus defined in Section 3.1.

The global ILF obtained by co-adding each ILF computed in each annulus (2 to 5) is presented in Figure 14. The two lines represent the observed ILF before (dashed line) and after (solid line) the correction for completeness, respectively. Errors have been computed accordingly to the following relation:

$$\sigma_{\text{bin}} = \left[\frac{N^{1/2}}{\Phi} + \frac{N \cdot \sigma_{\Phi}}{\Phi^2} \right] \quad (1)$$

where N is the number of stars effectively observed in each bin, Φ the completeness factor, and σ_{Φ} the associated error which was determined from the r.m.s. of the repeated completeness trials (typically less than 0.05).

In the same way, Figure 15 reports the ILF normalized to the total number (107) of RGs in the statistically decontaminated sample (NILF). The global uncertainty of the NILF in each bin depends also on the statistics of the number of RGs used to normalize the ILF, accordingly to the

relation:

$$\sigma_{\text{NILF}} = \left[\frac{\sigma_{\text{bin}}^{\text{ILF}}}{N_{\text{RGs}}} + \frac{N_{\text{ILF}} \cdot \sigma_{\text{RGs}}}{N_{\text{RGs}}^2} \right] \quad (2)$$

where N_{RGs} is the number of RGs adopted for normalization, $\sigma_{\text{bin}}^{\text{ILF}}$ is the error in each bin of the ILF obtained from eq. (1) and N_{ILF} is the number of MS stars in each bin of the ILF.

4.2.1. Comparing the NILFs

In Figure 16 we compare the MS NILF, computed adopting our sample, with the ones published in previous papers. We considered each of the region covered by previous papers on its own (see Figure 7). IN order to emphasize the number of RGs adopted in each region to normalize the MS ILF, we briefly summarize the above results: the actual number of RGs found by our photometry in each area surveyed by previous photometries are, respectively: 40,53 and 65 in the C89, B89, and BCP94 area. Accordingly to the adopted field population and the relative area extensions, we expected 1,4, and 6 field stars, respectively, in the CLUSTER RGs sector of the CMD. This yields a final number of 39, 49 and 59 RGs, which were used to normalize the MS ILF. It is particularly interesting to note that, apparently, both B89 and BCP94 did not apply any correction in order to take into account the field star contamination to the number of RGs. This correction is particularly large (6 RGs) in the area covered by BCP94.

The original NILF for the three published samples have been reported (as dashed lines) for comparison in Figure 16. They have been measured directly on the original published figures since none of the various authors reported the adopted LF in form of a list, and we could not reconstruct the completeness correction and the decontamination procedure applied by the authors to the observed samples. However, beside differences in the limiting magnitude, techniques and procedure, the NILF obtained in this paper agrees, within the uncertainties, with those published by previous studies at the bright end of the NILF ($V < 19$). Also, the fact that the decontamination procedure has not been applied to the B89 and BCP94 original sample does not seem to have affected the NILF, probably because, in both studies, the authors systematically over-estimate the completeness correction for MS stars.

Finally, we report the original NILF from C89 and BCP94 in Figure 17. The NILF obtained by B89 is not reported because it is fully consistent with the one from BCP94 by which it is superseded. We also draw, for comparison, the global NILF obtained for the whole adopted sample (plotted in Figure 15). The NILFs agree with each other, thus suggesting that the procedure adopted for the field decontamination and completeness correction does not introduce any substantial bias in the derivation of the NILFs. There is a weak indication that the NILF obtained from the C89 area is slightly more populated, but this should be regarded as an effect of statistical fluctuations. In fact, given the error bars, the three distribution are fully consistent within 1σ , and if the normalization

factor of C89 is enhanced from 39 to 41, the relative LF matches almost perfectly the others. On the basis of Figure 16 and Figure 17, we can conclude that the statement by BCP94 that the differences in the observed NILFs were due to statistical fluctuations in the choice of the samples seems confirmed.

5. Comparison with theoretical models

5.1. Preliminars

In order to compare the present data with theoretical models, some issues such as metallicity, distance modulus, and metallicity must be discussed. In the next paragraph we report some of the most recent determinations, as well as our final choices.

Metallicity: Most recent determinations of metallicity for NGC 1866 (Oliva and Origlia 1998; Hilker et al. 1995) attribute to the cluster a value $[Fe/H] \sim -0.55 \pm 0.30$. It should be noted that Hilker et al. (1995) performed a relative calibration of NGC 1866 on NGC 330, so that, depending on the value estimated for the latter cluster, the metallicity of NGC 1866 can be enhanced to $[Fe/H] \sim -0.35$.

Reddening: Values of $E(B-V)$ from the literature span from 0.05 (Walker 1992) to 0.10 (Elson 1991). Most authors, anyway, adopt $E(B-V) = 0.06$ (Walker 1974; Cassatella et al. 1987, B89).

Distance Modulus: The distance of the LMC is subject of controversy within the astronomical community. Even since the HIPPARCOS results, the problem is far from being solved once for all. The current values for the distance modulus span from 18.06 (Stanek et al. 1998) -which is, however, an outlier- to 18.70 (Feast and Catchpole 1997). Useful reviews of recent results on the distance modulus of the LMC can be found in Madore and Freedman (1998), Feast (1999) and Walker (1999).

In the following discussion, we adopt $Z = 8 \times 10^{-3}$ ($[Fe/H] \simeq -0.4$), $Y = 0.26$, and two visual distance moduli, namely $(m - M)_V = 18.6$ and $(m - M)_V = 18.8$, while the reddening will be assumed to vary between 0.06 and 0.10 (which means that the true distance modulus will range at most between 18.3 and 18.6, having adopted $A_V = 3.2E(B - V)$).

5.2. The analysis

We will focus our discussion on the LF because it provides a more robust tool than the distribution of the stars in the HR diagram (since it does not use the radii or, alternatively, the effective temperatures of the models, i.e. colors). Since we want to minimize the influence of the corrections for crowding on the observed LF, we limit our analysis to the region brighter than $M_V = 2.6$. In fact, down to this magnitude, the global corrections (which have been included!) to each bin are

always smaller than 10%, with only annulus 2 being corrected for a factor 40% in the faintest bin. The global correction to the total is constrained below 8% (see sect. 3.3 and 3.4).

The theoretical models have been computed with the evolutionary code FRANEC, whose earliest and latest versions are described, respectively, in Chieffi and Straniero (1989) and Chieffi et al. (1998), while the latest input physics are described in Straniero et al. (1997). Most models used here have been published by Dominguez et al. (1999), while others have been especially computed for this work. The models computed with an artificially enlarged convective core (hereinafter AECC models) have been obtained by increasing the size of the convective core by an amount equal to $0.25H_p$. We refer to such models as AECC and not as models computed with overshooting, since the fit to this (or another) cluster can only give us information about the probable size of the convective core, not about the mechanism which determines this size, as mentioned above.

All the theoretical luminosity functions have been obtained by means of a code which produces the synthetic clusters (O. Straniero et al., in preparation): this is a sophisticated tool which can manage a) the photometric errors, b) the effect of the crowding, c) the presence of binary systems having an arbitrary mass ratio, d) an age spread, e) an arbitrary initial mass function and f) a large number of photometric bands. Synthetic CMDs can be produced in the age range from few Myr up to several Gyr. All the models of which our evolutionary database range from the main sequence up to the advanced stages of interest for this work, so that no artificial match between different evolutionary phases is necessary.

The various studies of the LF of NGC 1866 available in the literature make use of the NILF, as discussed previously. Such approach was certainly valid in the previous studies of this clusters since a solid and complete MS extending over several magnitudes was not available. We have used the NILF in the previous sections in order to have a common ground with the previous papers on the subject. However, since we now have a well-defined (and essentially complete) MS down to at least 3 mag below the TO, we have a chance to adopt the MS itself as “normalization factor” instead of the He burning stars. Our synthetic CMDs are populated until the observed total number of stars brighter than $M_V = 2.6$ is reached and NOT until the total number of giants observed is reached. We believe this choice is, whenever possible, preferable to the other because: i) the total number of stars brighter than the quoted magnitude is largely independent on the assumed size of the convective core, since it is dominated by MS stars whose LF is only marginally affected by the size of the convective core; ii) the number of MS stars is much larger than that of the giants and is therefore much less affected by stochastic fluctuations. It must be noted, however, that the total number of stars brighter than the quoted magnitude depends on the adopted distance modulus (since it influences the limiting magnitude where we stop the counting), on the adopted present mass function (hereinafter PMF), and on the fraction of binary systems present in the cluster. We will discuss this below. The observed total number of stars brighter than $M_V = 2.6$ in our sample, corrected for completeness, is 4004 for the visual distance modulus $(m - M)_V = 18.6$ and 4362 if $(m - M)_V = 18.8$ is adopted; the total number of giant stars is 107.

Before discussing the fit to NGC 1866, we think it important to discuss the dependence of the theoretical LF on various parameters. Panels a) and b) in Figure 18 show, respectively, the differential and the integrated main sequence LFs for three ages, 80 (solid), 120 (dotted) and 160 (dashed) Myr. Clearly, the TO luminosity declines as the age increases while the overall shape of the LF around the TO remains substantially unaltered within the considered age range. Panels c) to h) in the same figure present the same LFs shown in the first two panels, but with the inclusion of the giants: from these panels emerges that the clump luminosity also dimmers as the age increases. It should be noted that the distribution of the stars within the clump shows a double peak which flattens as the age increases. This behavior is easily comprehensible if we consider that the stars spend most of their He burning lifetime either at the red dip minimum and at the blue nose of the blue loop, not in the middle. Since the older the isochrone the smaller the blue loop, it is also clear that the double peak feature disappears as the age increases. Another clear feature in Figure 18 is the magnitude gap between the TO and the red giant clump. This gap reduces as the age increases, because the clump luminosity dimmers faster than the TO (see Castellani et al. 1990). Figure 19 shows, for the same three ages, the effect produced by an increase of a factor of two in metallicity on the differential LF: the left and right panels show, respectively, the MS and the total LF, while the solid and dotted lines refer, respectively, to the larger and the reference metallicity. The end effect of an increase of 0.3 dex in metallicity is a simulation of an older age; in fact, the clump luminosity becomes fainter, and both the double peak feature within the clump and the gap between the TO and the clump itself are reduced, while the TO becomes more luminous; the latter feature implies that the larger metallicity requires an older age in order to have the same TO luminosity.

The influence of the size of the convective core on the LF can be readily seen in Figure 20 where the solid lines refer to the AECC case while the dotted ones refer, once again, to the reference case. The increase in mass of the convective core has a deep impact on the LF: the region around the TO is modified because the TO luminosity increases and the AECC LF is much steeper around the TO. Also, the clump is significantly affected by the AECC, since it appears to be brighter and flatter. It is interesting to note how the synthetic diagrams populate the respective isochrones. Figure 21 shows in each panel a different isochrone superimposed onto its synthetic diagram obtained by choosing a number of stars equal to the sample observed in NGC 1866, i.e. 4004 stars brighter than $M_V = 2.6$. The upper and lower panels refer, respectively, to the two ages $t=100$ and $t=200$ Myr, while the left and right panels refer, respectively, to the reference (standard) and AECC isochrones. The MS stops being populated before the formal "theoretical" TO; this is due to the fact that these clusters (and NGC 1866 is even one of the most populous ones!) are not rich enough to significantly populate the isochrone around the TO. The effect is only marginally present in the standard case, but it is dramatic when the AECC model is considered. As a consequence, the difference between the two M_V^{TO} (standard and AECC) is largely reduced if evaluated on the synthetic diagrams (i.e. on the basis of the most brilliant MS star) rather than on the isochrones. Let us explain this point in detail: the region between the small MS hook (see Figure 21) and the "theoretical" TO is populated by stars which are in the so-called *overall contraction* phase: during this phase, the stars

shift from a structure controlled by a central burning to one controlled by a shell burning. The evolutionary timescale of this phase is largely determined by the size of the He core mass (which directly depends on the size of the convective core), in the sense that it scales inversely with the size of the He core. Thus, the larger the He core mass (i.e. the larger the previous convective core), the faster the evolution between the MS hook and the TO (and hence the lower the expected number of stars in this region): this explains why synthetic CMDs obtained by assuming a larger convective core have the TO region of the isochrone underpopulated with respect to the standard case.

The last effect we want to show is connected to the likely presence of a significant fraction of binaries. It has been recently found with HST observations (Elson et al. 1998) that NGC 1818, a cluster similar to NGC1866, but slightly younger, has a conspicuous population of binary systems estimated of the order of 30%.

In our analysis, the presence of binaries is taken into account as follows: 1) the mass of the first star comes, as usual, from a random extraction weighed with a PMF having the same slope α used in the extraction of the single stars, 2) the mass of the companion is extracted by assuming a gaussian distribution (of the masses) with a peak mass equal to that of the first star. In this particular case, we chose a rather narrow gaussian distribution (semidispersion equal to 0.1), in order to maximize the effects due to the binary population. Clearly, the effect on the luminosity of the compound system is maximized if the two stars have similar masses because, otherwise, one of the two would dominate and the total luminosity would practically be that of the most luminous of the two. By the way, such an occurrence clarifies why the crowding behaves in principle similarly to real binary systems but is, in practice, quantitatively less effective: in fact, once the fraction of “binaries” is fixed, if one assumes that they are all due to the crowding, the masses (i.e. the luminosities) involved in the formation of the “binary system” are not constrained by any rule to be similar, and hence, as a consequence the less luminous of the two is hidden by the other which, in turn, will remain essentially unmodified.

Figure 22 shows in the left panel a comparison between the integrated LF of the main sequence in the reference case (thin line, hereafter MSILF), and the one obtained including a 30% of binaries (thick line) for an age of 120 Myr and a mass function slope $\alpha = 2.3$. The inclusion of a significant fraction of binaries alters the LF by flattening the MS slope and steepening the LF of the TO region. This means that the presence of the binaries masks the real slope of the PMF, in the sense that it appears flatter than it really is. The right panel shows, for example, how the reference MSILF already shown in the left panel (computed with $\alpha = 2.3$) is well reproduced by the one computed with $\alpha = 2.6$ and a 30% of binaries. Such occurrence will have a significant impact on the fit to the cluster (see below).

With the aid of the theoretical scenario discussed above, we can now readily turn to the analysis of NGC 1866. In particular, we shall first show the fits with the standard and AECC models, and we shall then discuss how they change by including a 30% of binaries.

5.2.1. Classical analysis with standard models

The comparison between our standard models and NGC 1866 is summarized in Figures 23 to 26 for the assumed distance modulus $(m - M)_V = 18.6$. In Figure 23 we report, for the three ages 100, 120 and 140 Myr and five values of the PMF slope ($\alpha = 2.0, 2.1, 2.2, 2.3, 2.4$), the comparison between the theoretical MSILF (histogram) and the cluster data (black dots). Although this is a standard way of comparing the theoretical and the observed integrated luminosity functions, we think it difficult to judge the goodness of a specific fit. Hence we computed, for each case shown in Figure 23, the differences (observed-theoretical), in units of $\sigma = (N_{obs} - N_{theo})/(N_{theo})^{1/2}$. These are shown in Figure 24. Hereafter, we will refer to this quantity as $\Delta\sigma$. Since it will constitute the basis on which we shall determine both the age and the PMF slope, α , we discuss it in brief: as the total number of stars brighter than $M_V = 2.6$ is equal to the observed number, the first point to the right end of each panel always corresponds to $\Delta\sigma = 0$ (i.e. theoretical and observed number are identical). Moving toward brighter magnitudes, the other values for $\Delta\sigma$ will not necessarily remain around the zero (good match) but their trend with the magnitude will depend on the current adopted values for both α and the age: the larger the range in magnitude over which $\Delta\sigma$ remains close to zero, the better the fit. Now, let us consider the various rows in Figure 24: the three panels in each row have been obtained by assuming a constant PMF slope and the three adopted ages. As a general trend, an age increase tends to globally lower the sequence of points. By looking along the columns at Figure 24, one can see the effect of a changing α at fixed age. In this case, the global trend of $\Delta\sigma$ is toward lower values as α increases. If we focus on the first column in Figure 24, we can see that, for an age of 100 Myr, an increase in α from 2.0 to 2.2 improves the fit: all the points move down toward zero and a good match is obtained in the magnitude range 1.5-2.6; a further increase of α worsens the fit because the points corresponding to the brightest part of the MS still tend to move down toward zero, whereas those which were previously close to zero move progressively below it. Since, even in the best case ($\alpha = 2.2$), only a very small part of the MS can be fitted, we conclude that, for this age, models cannot fit the data well enough. The same general behavior is obtained for the other two ages too; in particular, for $t=120$ Myr the "best" fit is obtained for α of the order of 2.2-2.3, while for $t=140$ Myr the "best" match corresponds to $\alpha \sim 2.1$. At variance with the 100 Myr case, however, there is a good fit all along the magnitude range from -0.5 to 2.6 for both these ages. By increasing the age above 140 Myr one obtains a situation similar to the one discussed for 100 Myr: no good fit is obtained for any value of α over a reasonably extended magnitude interval of the MS. By adopting a visual distance modulus of 18.6, we conclude that it is possible to constrain the age of this cluster in the range 120-140 Myr with α in the range 2.1-2.3, depending on the age. It is worth noting that, by means of this technique, we have been able to constrain the age without using -so far- the TO luminosity: on the contrary, we have shown (and used) that the part of the MS down to 3-4 magnitudes below the TO depends significantly on the age; an age derived in this way is much more robust than the one obtained by a fit to the most luminous MS stars, because these stars are very few and hence are subject to heavy stochastic fluctuations. The further fit to the TO luminosity remains confined within the age range found above. The various panels in Figure 24 show that, in no case, it is possible to obtain

a good fit to the ILF near the TO region. Standard models predict a smooth decline of the ILF toward the brightest portion of the MS while the observed ILF shows a much steeper profile. Since the theoretical ILFs preserve such a shape around the TO over an extended age range, we will not obtain a good fit for any standard model in any -reasonably wide- age range.

We can now extend our analysis to the post main sequence evolution, i.e. the core He burning phase. In Figure 25 and Figure 26 we show, respectively, the differential and integrated LFs of the total sample. By looking at the panels corresponding to the cases showing a good fit to the MS (see above) we find that, while the average clump luminosity is reasonably well reproduced, there are a number of discrepancies which can hardly be reconciled: in particular, the models predict a number of clump stars which is almost twice the observed one and also a significant (~ 0.6 mag) luminosity gap between the TO and the He clump, which is not observed. We therefore conclude that it is impossible to obtain a reasonable fit to NGC 1866, having assumed a visual distance modulus of 18.6, with the use of standard models.

The same analysis has been made for a visual distance modulus of $(m - M)_V = 18.8$. The logical steps followed to perform the fit are the same adopted for the shorter distance modulus. In this case, we obtained a good fit to the MS only for $t = 100$ Myr, $\alpha = 2.0$, and $t = 120$ Myr, $\alpha \sim 1.9$, while there is no good fit for ages outside this range, whichever α is used. We show the best fit for this case in Figure 27. The same discrepancies already evidenced for the shorter distance modulus are still present: the shape around the TO region is not reproduced, nor are the total number of giants and the gap between the bright end of the MS and the clump. The adoption of a longer visual distance modulus does not improve the fit to the cluster, which remains rather poor.

We have thus obtained, once again, the classical old problem first raised by Becker and Mathews (1983): i.e. standard models predict much more He clump stars than observed, with the difference that the validating sample is now much larger.

5.2.2. Classical analysis with AECC models

The fit with AECC models is shown in Figure 28 to Figure 31 for the distance modulus $(m - M)_V = 18.6$. Now, a good fit to the MSILF is obtained in the age range 200-220 Myr and $\alpha \sim 2.1 \div 2.2$, but only for $t \sim 200$ Myr and $\alpha \sim 2.2$ there is also a reasonable fit to the TO. An analysis of the post MS evolution (Figure 30 and Figure 31) shows that the number of giants predicted for this "best" case is in good agreement with the observed one. However, it must be noted that the clump LF is not well reproduced since it is predicted to be, on the whole, less luminous than observed.

The increase of the visual distance modulus to $(m - M)_V = 18.8$ leads to a largely poorer fit. In this case, the MS may be fitted in the age range 180-200 Myr and α 's in the range 2.0-1.8, but in no case do we obtain a fair fit to the TO region. The best overall fit (shown in Figure 32) corresponds to $t \sim 180$ Myr and $\alpha \sim 2.0$. The number of giants predicted agrees with the observed ones, while

the synthetic LF remains systematically below the observed and shows a well-defined gap between the clump and the brightest MS stars, which is not observed (panels c) and d) of Figure 32).

We conclude that the AECC models may fairly fit the observed LF only if a "short" distance modulus is adopted.

5.2.3. *Non classical analysis with standard models*

We now discuss the influence that a consistent fraction of binary systems (30%) has upon the fit to a cluster like NGC 1866. As mentioned above, this value has already been found in NGC 1818, by means of HST observations, and hence it is a reasonable starting value.

A good fit to the MS is obtained for $t = 120 \div 140$ Myr and α between 2.4 and 2.6 when a distance modulus $(m - M)_V = 18.6$ is assumed. Although for both ages the shape around the TO is relatively well reproduced, an age of 120 Myr and $\alpha = 2.5$ give the best fit to the data (see panels a) and b) in Figure 33). Note that, at variance with the case without binaries, we now have a good fit to the TO region too, because the presence of the binaries tends to steepen the ILF toward the bright end of the MS (see above). A further analysis of the giant stars is partly contradictory: while the predicted number of giants (148) is $\sim 4\sigma$ larger than observed (107), the clump luminosity is reasonably well reproduced (see panels c) and d) in Figure 33).

By increasing the distance modulus to 18.8, we obtain a really good fit (shown in Figure 34) for an age $t = 100$ Myr and $\alpha = 2.4$. The whole MS sequence, including its bright end, is well reproduced. The post MS evolution is also fairly well reproduced (see panels c) and d) in Figure 34): the number of giants predicted is within 2σ of the observed number and, even more important, the luminosity distribution of the giants closely matches the observed ones.

In conclusion, the adoption of models computed with a standard extension of the convective core may lead to a good fit to NGC 1866 if we account for a non negligible population of binary systems ($\simeq 30\%$) and adopt the "long" visual distance modulus (i.e. $(m - M)_0 = 18.5 \div 18.6$). The TO mass predicted for this "overall globally best" case is $4.5 M_\odot$, while the He clump mass is around $4.8 M_\odot$.

5.2.4. *Non classical analysis with AECC models*

For sake of completeness, we also consider the case of AECC models with a 30% of binaries. A good fit to the entire MS and the TO is now obtained for an age range $t \simeq 220 \div 240$ Myr and $\alpha \simeq 2.4 \div 2.6$, if $(m - M)_v = 18.6$ is assumed (see panels a) and b) in Figure 35). The number of predicted giants closely matches the observed one. Nonetheless, this fit must be rejected because the luminosity of the clump stars is largely missed: panels c) and d) in Figure 35 clearly show that the sum of the two effects, i.e. larger convective cores and a 30% of binaries, leads to predicted

giants with a luminosity far too weak in comparison with the observed ones. The adoption of the longer distance modulus, which is not shown, does not improve at all the fit since, here too, the “theoretical” He clump is largely underluminous with respect to the observed one.

We conclude that the simultaneous inclusion of a binary component, together with the use of AECC models, does not provide an acceptable fit to the observed LF of this cluster.

Before closing this section, we shall comment the so-called NIMSLF (i.e. Normalized Integrated Main Sequence Luminosity Function) for the cases obtained by including a binary component. Panels e) in Figures 33 to 35 show the comparison between the observed (black dots) and synthetic (histogram) NIMSLFs; the open dots correspond to a 2σ changing in the observed NIMSLF. Since this kind of figure gives a pivotal role to the number of giants, the fit obtained with the AECC+binary models clearly leads to the best fit. We have, however, shown that a deeper analysis, i.e. one which addresses all the features available in the observed LF, leads to the conclusion that this case must be rejected. On the contrary, the fit obtained by adopting the standard models plus the binary component, although it gives a worse fit to the observed NIMSLF (they agree within 2σ), leads to a reasonably good fit to this cluster.

6. Summary and conclusions

In this paper, we presented a new set of photometric data which largely increase the samples presented up to now. We have also shown systematically how the various theoretical models and/or scenarios can fit the observed data. As a first conclusion, we find that the discrepancy first evidenced by Becker and Mathews (1983), i.e. that standard models predict an excess of He clump stars, is still present even with the latest standard models. The easiest and most straightforward way to avoid the discrepancy is to artificially increase the size of the convective core. Unfortunately, a side-effect connected to the use of AECC models is a fainter clump luminosity. If the convective core is larger, an older age is needed in order to fit the bright end of the MS, but in this case, the isochrone displays a fainter He-burning clump.

Another method used to reconcile the theoretical predictions with the present set of data is to take into account the possible presence of a fraction of binary stars. Already C89 temptatively tried to check the effect of the presence of a binary population on the fit to their NILF. They concluded that the inclusion of even 50% of binaries did not significantly alter the fit and, hence, binaries were not relevant for the understanding of NGC 1866. A look at fig. 18 of C89 shows that the inclusion of binaries increases significantly the NILF, although not enough to match the observations. Nevertheless, from that figure it was possible to show that binaries mimic (of course only from this point of view) an enlarged convective core: the observed ratio N_{MS}/N_{He} is increased. This effect was also noted by B89, who clearly stated in their final discussion that the presence of the binaries could mimic the effect of the overshooting on the NILF, and lead to a closer agreement between (their) data and the standard models.

Note, however, that while models computed with AECC produce a fainter clump luminosity, models with binaries do not do so. Binaries alter a synthetic diagram in two ways: they overpopulate the bright end of the MS (thus reducing the ratio N_{MS}/N_{He}) and require a steeper “intrinsic” PMF slope. This implies that, with a fixed total number of stars to be extracted, less massive stars are favored with respect to those around the TO and beyond: hence the predicted number of giants is reduced.

By including a fraction of 30% of binaries, we have shown that standard models can nicely fit the data. Of course, one could question the real occurrence of binary systems in NGC 1866. We have, in fact, two alternative scenarios:

a) if there are essentially no binary systems in NGC 1866, only models computed by significantly increasing the size of the convective core can fairly fit the present sample of data. In this case, however, we are still faced with the fact that it is impossible to fit the luminosity function of the clump stars. Such discrepancy increases together with the distance modulus. In this scenario, the age of NGC 1866 would be $t \simeq 200$ Myr and the PMF slope $\alpha \simeq 2.2$;

b) if there is a conspicuous fraction of binary systems, standard models provide a good fit to the present data. In this case, however, the preferred visual distance modulus is $(m - M)_V = 18.8$, i.e. $(m - M)_0 = 18.5 \div 18.6$, depending on the adopted reddening. In this scenario, the age is $t \simeq 100$ Myr and the intrinsic PMF slope, α , of the order of 2.4.

The choice between these two alternative scenarios can be done either by solving the problem of the distance modulus, because for each given modulus only one of them is favored, and/or by improving our knowledge of the fraction of binary systems existing in NGC 1866.

In our opinion a real advance in the knowledge of this (and maybe other) class of objects requires an observational effort for a real determination of the fraction of binaries present in the cluster, more than a further increase in the data sample (which is, however, always welcome). As final remark, we hope that the incoming Cycle 8 HST observations will finally solve the enigma of NGC 1866.

7. acknowledgements

We gratefully acknowledge Enzo Brocato, Cesare Chiosi and Antonella Vallenari for giving us computer-ready tables of their published photometries and their isochrones, and for helpful discussions. We warmly thank Giuliana Giobbi for editorial help, and the anonymous referee for useful comments.

REFERENCES

Arp H.I., Thackeray A.D., 1967, ApJ, 149, 73

- Becker S.A., Iben I Jr., 1979, *ApJ*, 232, 831
- Becker S.A., Mathews G.J., 1983, *ApJ*, 270, 155
- Bertelli G., Mateo M., Chiosi C., Brressan A., 1992, *ApJ*, 388, 400
- Bolte M., 1989, *ApJ*, 341, 168
- Brocato E., Buonanno R., Castellani V., Walker A.R., 1989, *ApJS*, 71, 25
- Brocato E., Castellani V., Piersimoni A.M., 1994, *A&A*, 250, 59
- Cassatella A., Barbero J., Geyer E.H., 1987, *ApJS*, 64, 83
- Castellani V., Giannone P., Renzini A., 1971, *Ap&SS*, 10, 355
- Castellani V., Chieffi A., Pulone L., Tornambé A., 1985, *ApJ*, 294, L31
- Castellani V., Chieffi A., Straniero O., 1990, *ApJS*, 74, 463
- Chieffi A., Straniero O., 1989, *ApJS*, 71, 47
- Chieffi A., Limongi M., Straniero O., 1998, *ApJ*, 502, 737
- Chiosi C., Bertelli G., Meylan G., Ortolani S., 1989, *A&A*, 219, 167
- Cox A.N., Tabor J.E., *ApJS*, 31, 271
- Dominguez I., Chieffi A., Limongi M., Straniero O., 1999, *ApJ*, accepted (astro-ph/9906030)
- Elson R.A.W., 1991, *ApJS*, 76, 185
- Elson R.A.W., Sigurdsson S., Davies M., Hurley J., Gilmore G., 1998, *MNRAS*, 300, 857
- Feast M.W., 1999, *PASP*, 111, 775
- Feast M.W., Catchpole R.M., 1997, *MNRAS*, 286, L1
- Ferraro F.R., Carretta E., Corsi C.E., Fusi Pecci F., Cacciari C., Buonanno R., Paltrinieri B., Hamilton D., 1997, *A&A*, 320, 757
- Fischer P., Welch D.L., Côté P., Mateo M., Madore B.F., 1992, *AJ*, 103, 857
- Frogel J.A., Mould J.R., Blanco V.M., 1990, *ApJ*, 352, 96
- Hilker M., Richtler T., Gieren W., 1995, *A&A*, 294, 648
- Huebner W.F., Merts A.L., Magee N.H., Eargo M.F., 1977, Los Alamos Sci. Lab. Report (LA-6760-M)

- Lattanzio J.C., Vallenari A., Bertelli G., Chiosi C., 1991, *A&A*, 250, 340
- Madore B.F., Freedman W.L., 1998, *ApJ*, 492, 110
- Mateo M., 1998, *ApJ*, 331, 261
- Mighell K.J., Rich R.M., Shara M., Fall S.M., 1996, *AJ*, 111, 2314
- Oliva E., Origlia L., 1998, *A&A*, 46, 54
- Sandquist E., Bolte M., Stetson P.B., Hesser J.E., 1996, *ApJ*, 470, 910
- Stanek K.Z., Zaritsky D., Harris J., 1998, *ApJ*, 500, L141
- Stetson P.B., 1987, *PASP*, 99, 191
- Straniero O., Chieffi A., Limongi M., 1997, *ApJ*, 490, 425
- Walker A.R., 1992, *AJ*, 104, 1351
- Walker A.R., 1995, *AJ*, 110, 638
- Walker A.R., 1999, in *Post-Hipparcos Cosmic Candles*, ed. A. Heck and F. Caputo, Kluwer Acad. Publisher, p. 125
- Walker M., 1974, *MNRAS*, 169, 199
- Wood P.R., in *Frontiers of Stellar Evolution*, ed. D. L. Lambert, ASPCS Vol. 20, p. 213 110, 638

Fig. 1.— Computer map of the two fields (FA and FB) observed in the region of NGC 1866. The coordinates are in pixels (0.363 arcsec/pixel). In this system the cluster center is located at pixel (520,520). The circle (at $r \sim 6'$) delimits the FIELD sample (see text).

Fig. 2.— CMDs of stars in: *panel (a)* the CLUSTER sample (all stars in the field FA have been plotted); *panel (b)* the FIELD sample (all stars in the field FB with $r > 6'$ from the cluster center are plotted).

Fig. 3.— CMD for stars in the CLUSTER sample. The dashed lines delimitate three regions in the CMD mainly populated by CLUSTER MS stars, CLUSTER RGs, and FIELD RGs, respectively.

Fig. 4.— CMDs for annuli at increasing distance from the cluster center (*panels (a-e)*). The FIELD sample is plotted in *panel (f)* for comparison.

Fig. 5.— Mean photometric errors in V magnitude and (B-V) color, for annuli at increasing distance from the cluster center.

Fig. 6.— Completeness curves for the MS stars in the 5 annuli (1-5) at different distances from the cluster center as a function of the V magnitude as derived from *artificial stars experiments*

Fig. 7.— The maps of the regions selected by previous studies (B89, C89 and BCP94) to construct the LF, are reported over the FA field of view.

Fig. 8.— Comparison with previous photometries: C89. *panel (a)*: stars found in common; *panel (b)*: stars found only in our sample; *panel (c)*: stars detected only in C89. Only the region selected by C89 (see Figure 7) to construct their LF has been considered in the comparison.

Fig. 9.— Comparison with previous photometries: B89. *panel (a)*: stars found in common; *panel (b)*: stars found only in our sample; *panel (c)*: stars detected only in B89. Only the region selected by B89 (see Figure 7) to construct their LF has been considered in the comparison.

Fig. 10.— Comparison with previous photometries: BCP94. *panel (a)*: stars found in common; *panel (b)*: stars found only in our sample; *panel (c)*: stars detected only in BCP94. Only the region selected by BCP94 (see Figure 7) to construct their LF has been considered in the comparison.

Fig. 11.— Comparison between star counts obtained in the sample presented in this paper and the previous photometries (B89, C89, BCP94) *panel (a),(b),(c)*, respectively. Only stars in the MS sector of the CMD have been counted. No corrections for completeness or field contamination have been applied to these counts. Only the regions selected by each authors (see maps in Figure 7) to construct their LF has been considered in the comparison.

Fig. 12.— CMDs for annuli at different distance from the cluster center (annuli (1-5)) before (left-hand panels) and after (right-hand panels) the statistical decontamination procedure.

Fig. 13.— CMDs for stars in the final adopted sample (annuli (2)-(5)) after the statistical decontamination.

Fig. 14.— ILF for MS stars with (heavy solid line) and without (dashed line) completeness correction

Fig. 15.— ILF for MS stars normalized (NILF) to the total number of RGs. with (heavy solid line) and without (dashed line) completeness correction.

Fig. 16.— Comparison with previous MS ILFs : C89, B89, BCP94, in panel (a),(b),(c) respectively. NILF based on the sample presented in this paper is plotted as heavy solid line. The number of RGs adopted in the normalization in area has been reported in each panel.

Fig. 17.— Original MS-NILFs are plotted in the same panel to allow a direct comparison. Also plotted is (heavy solid line) the global NILF shown in Figure 15.

Fig. 18.— Dependence of the model differential (left panel) and integrated (right panel) LFs on the age. Age used are $t=100$ Myr (solid), $t=120$ Myr (dotted), $t=140$ Myr (dashed).

Fig. 19.— Dependence of the differential (left panel) and integrated (right panel) LFs on the metallicity. Lines refer to $Z=0.016$ (solid) and $Z=0.008$ (dotted)

Fig. 20.— Dependence of the differential (left panel) and integrated (right panel) LFs on the size of the convective core (overshooting). Solid lines refer to AECC models, dotted lines to standard models.

Fig. 21.— Synthetic CMDs populating their respective isochrones for models with standard core size (left column) and models with AECC (right column) and for two different ages.

Fig. 22.— Left panel: model MSILF with $\alpha = 2.3$ without binaries (dashed line) and with 30% of binaries (solid line). Right panel: the same standard case as in the left panel (dashed) is reproduced with 30% binaries and $\alpha = 2.6$ (solid).

Fig. 23.— Comparison between the theoretical MSILF (histogram) and the observed data (dots) in the standard case for three ages (columns) and five values of α (rows) and $(m - M)_V = 18.6$.

Fig. 24.— Comparison between the theoretical MSILF and the observed data in the standard case, in units of $\sigma = (N_{obs} - N_{theo})/(N_{theo})^{1/2}$. Rows and columns are as in Figure 23.

Fig. 25.— Comparison of the integrated theoretical and observed LF including the giant stars. Symbols and arrangement of rows and columns are as in Figure 23.

Fig. 26.— As in Figure 25 but for the differential LF.

Fig. 27.— The best fit obtained in the standard case for the “long” distance modulus $(m - M)_V = 18.8$.

Fig. 28.— Comparison between the theoretical MSILF (histogram) and the observed data (dots) in the AECC case for three ages (columns) and five values of α (rows) and $(m - M)_V = 18.6$.

Fig. 29.— Comparison between the theoretical MSILF and the observed data in the AECC case, in units of $\sigma = (N_{obs} - N_{theo})/(N_{theo})^{1/2}$. Rows and columns are as in Figure 28.

Fig. 30.— Comparison of the integrated theoretical and observed LF including the giant stars for the AECC case. Symbols and arrangement of rows and columns are as in Figure 28.

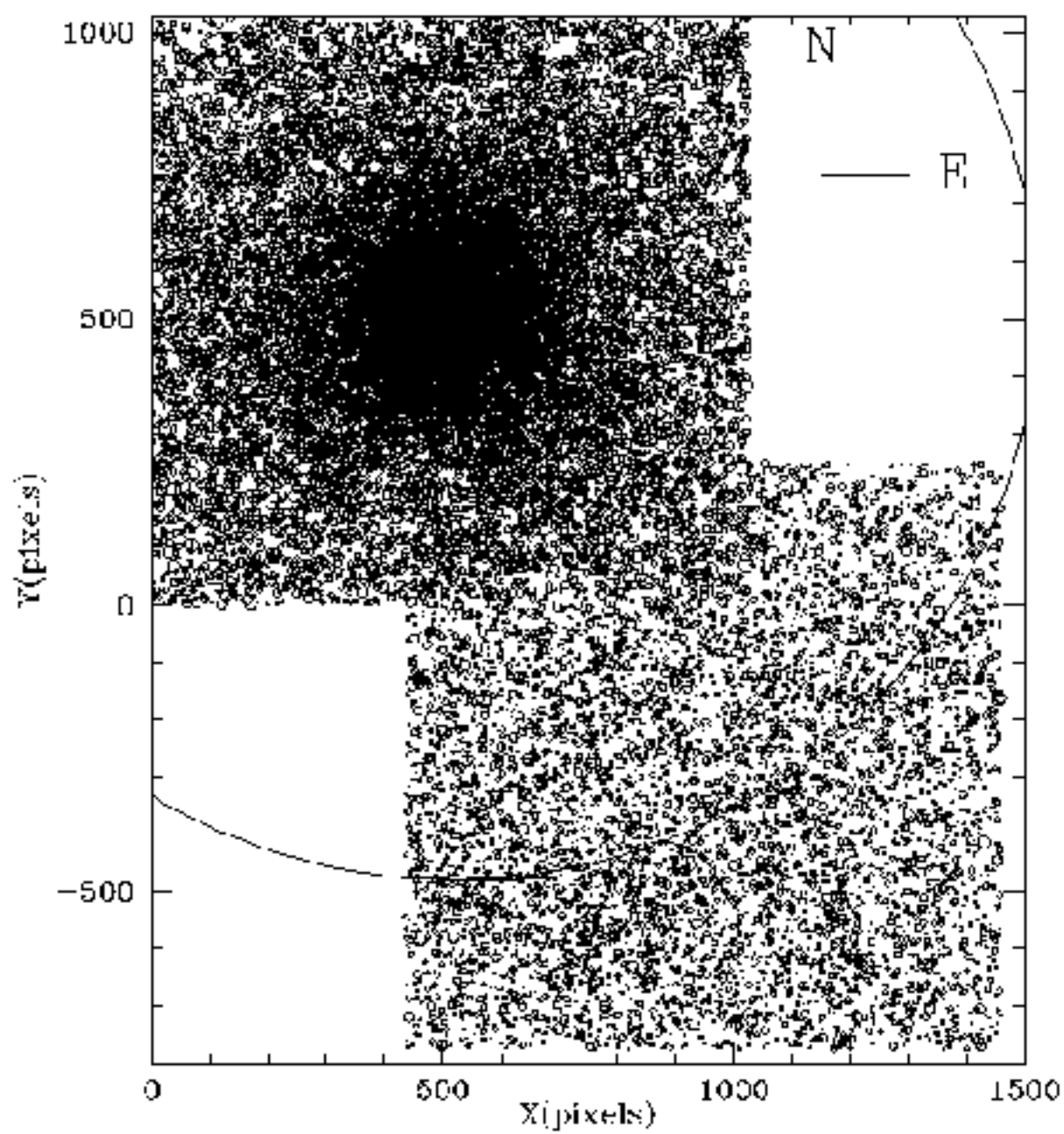
Fig. 31.— As in Figure 30 but for the differential LF.

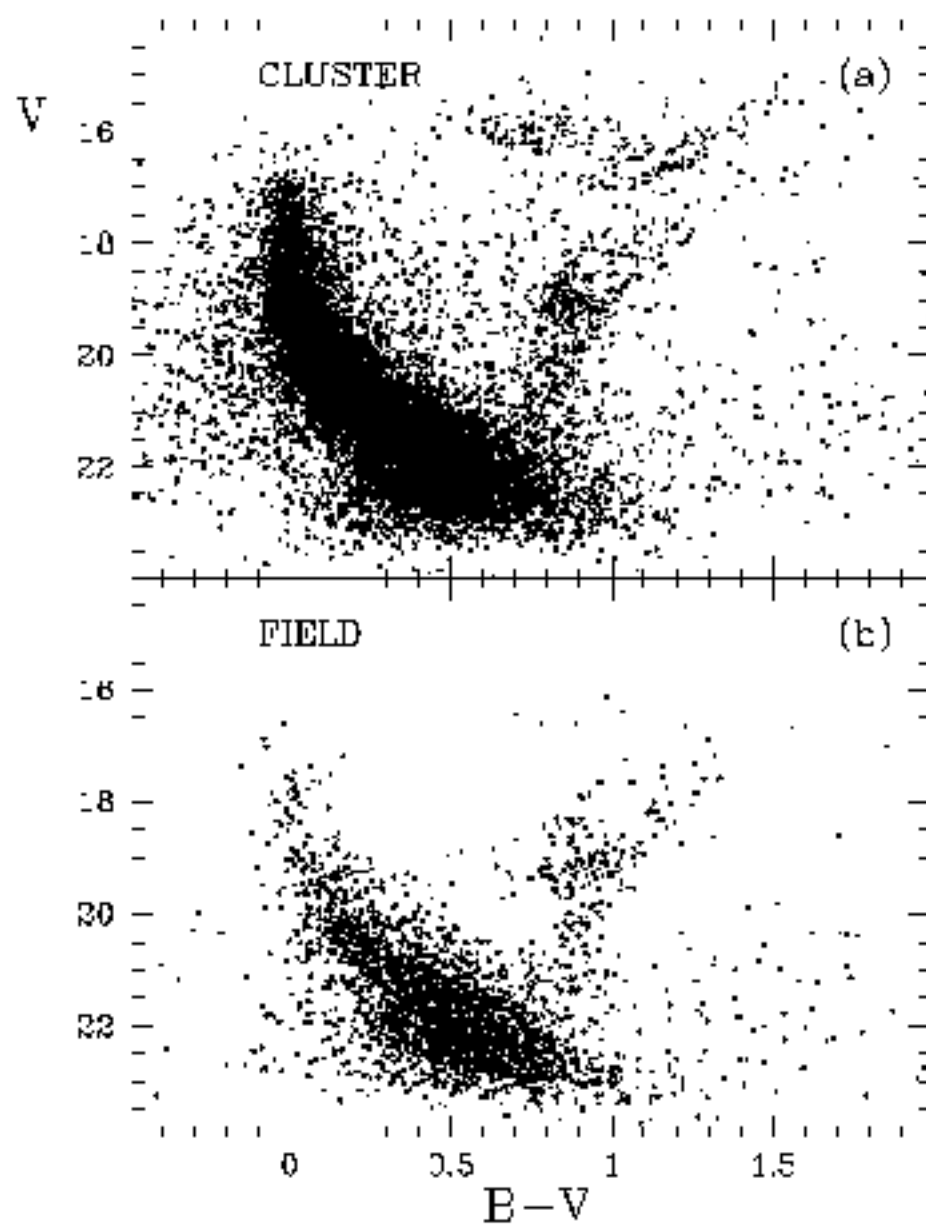
Fig. 32.— The best fit for the AECC case for the “long” distance modulus $(m - M)_V = 18.8$.

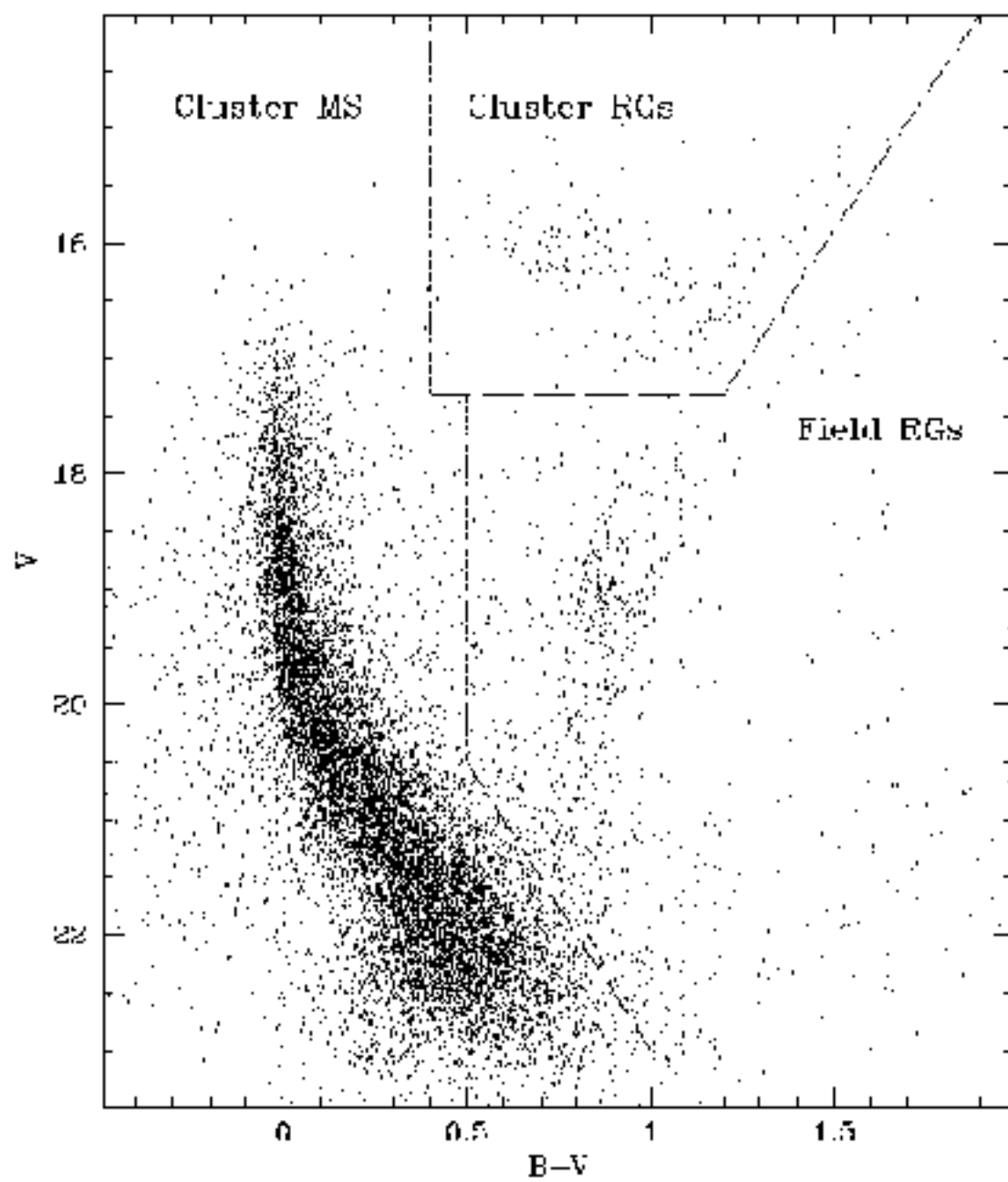
Fig. 33.— The best fit obtained for the standard+binaries case for the “short” distance modulus $(m - M)_V = 18.6$.

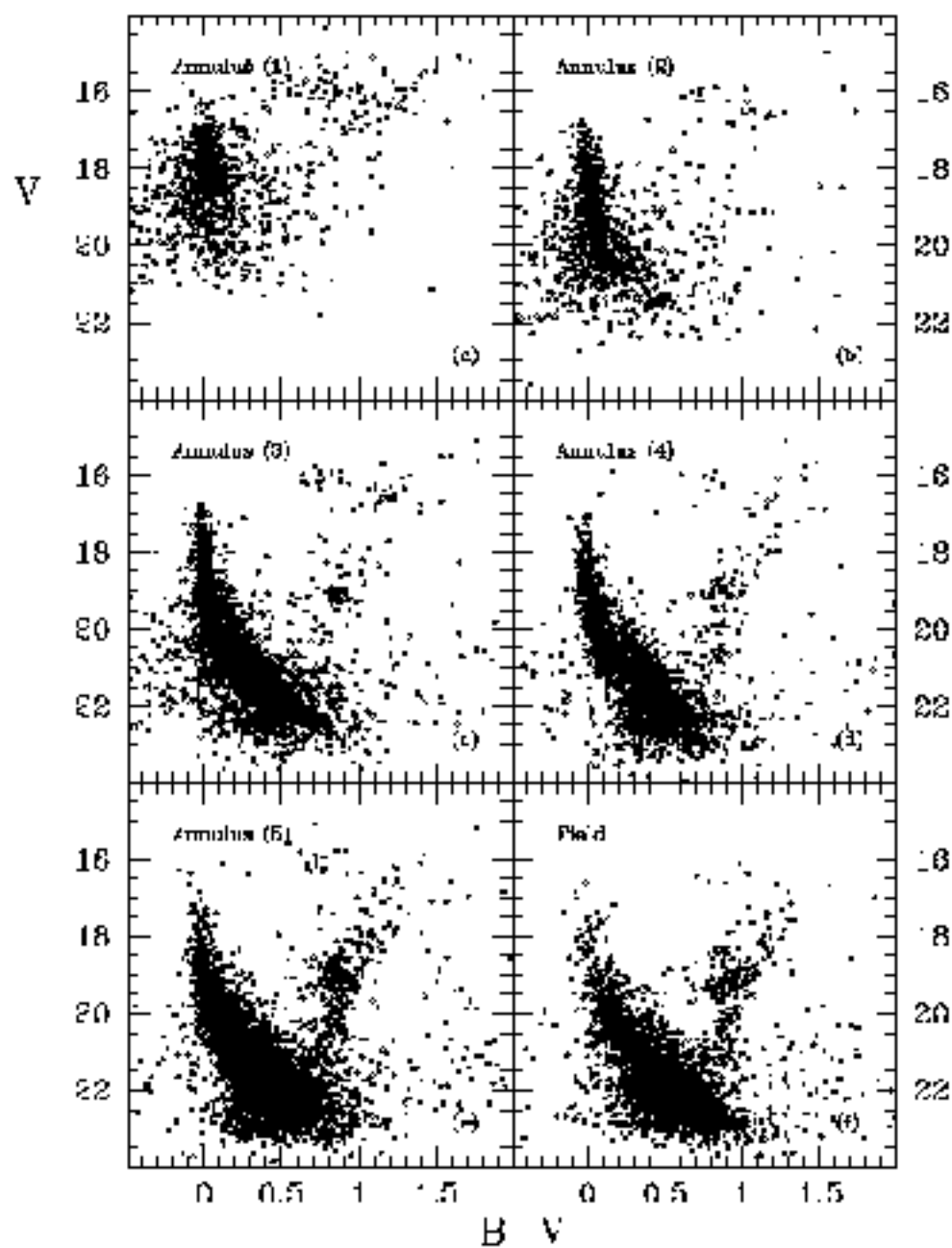
Fig. 34.— As in Figure 33 but for the “long” distance modulus $(m - M)_V = 18.8$.

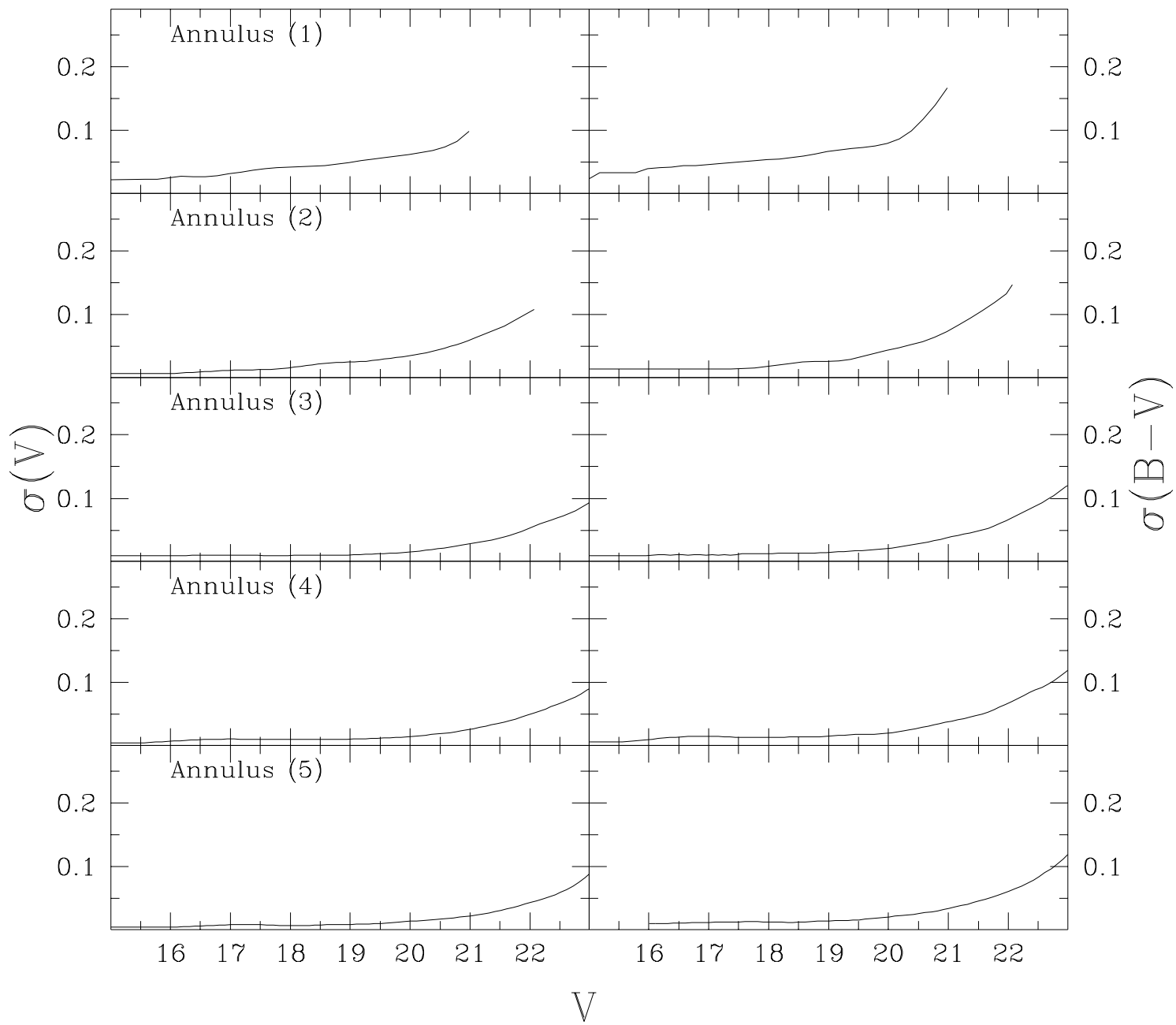
Fig. 35.— As in Figure 33 but for the AECC+binaries case.

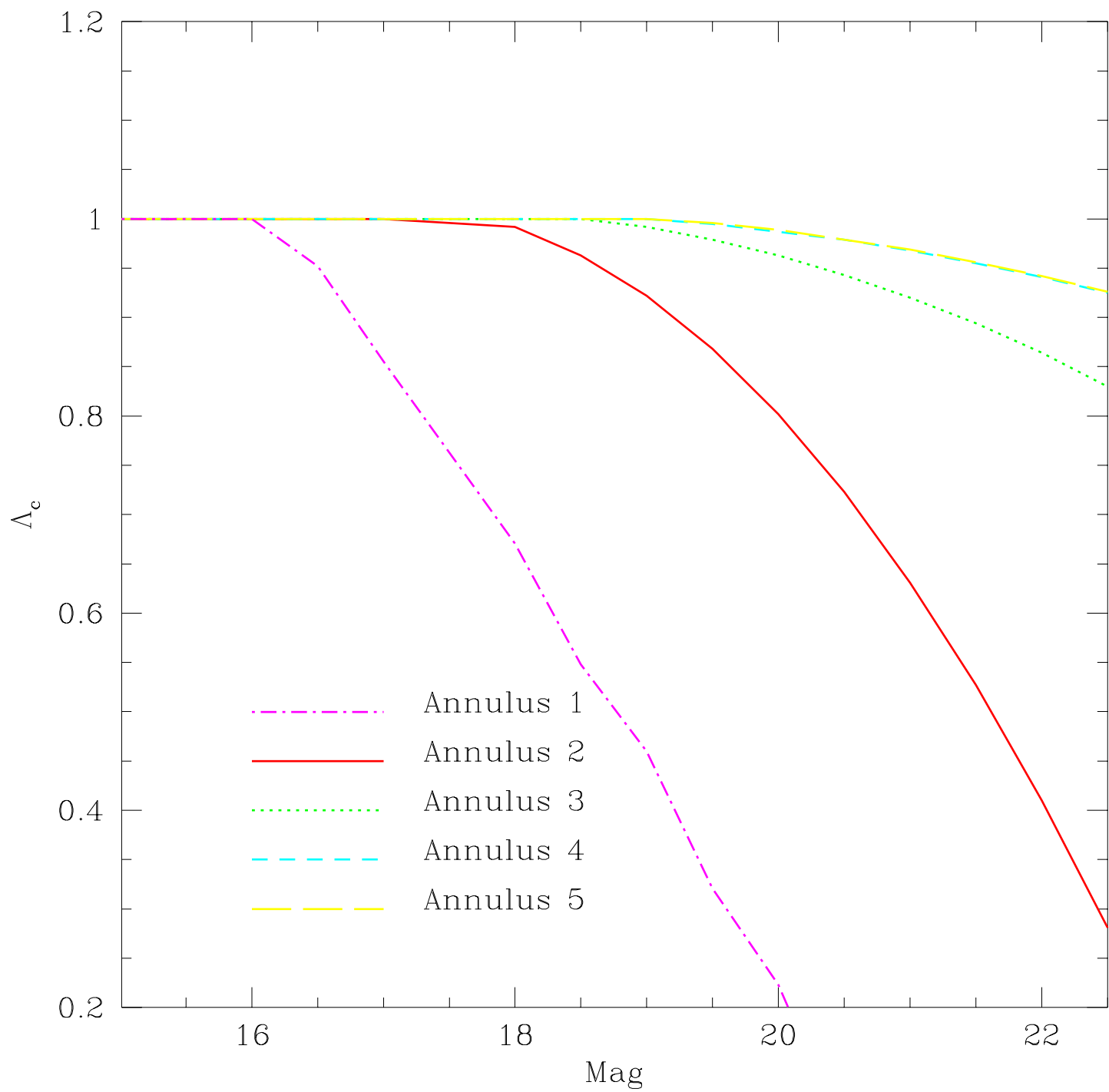


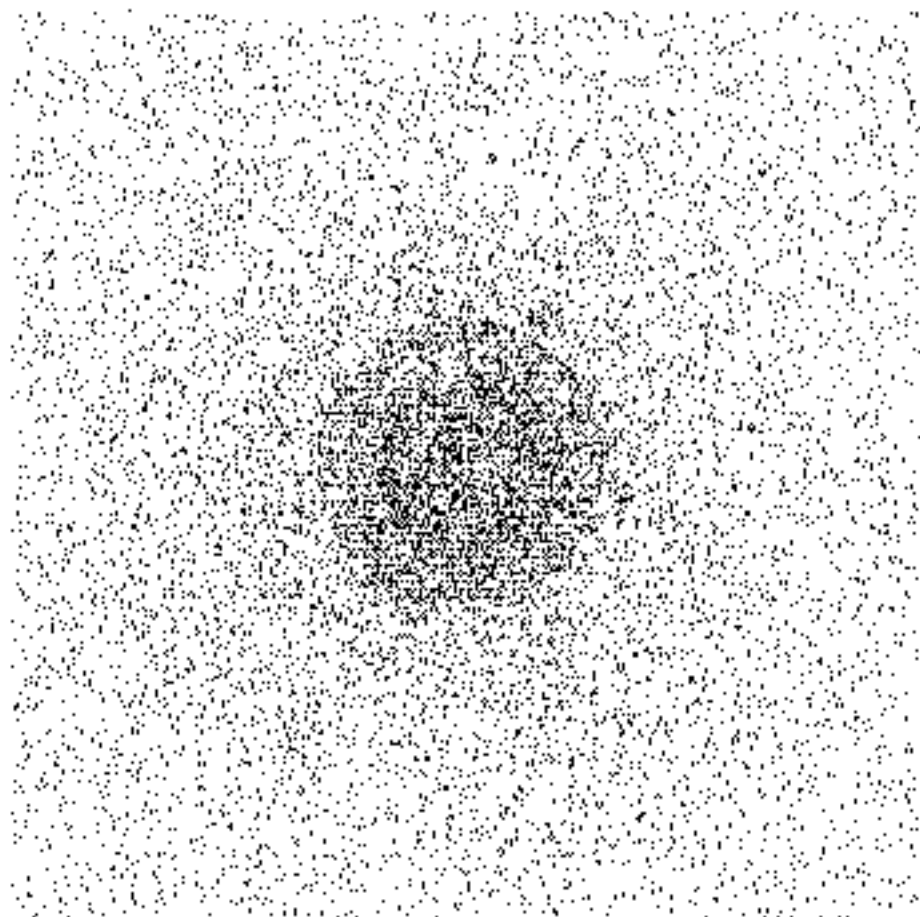


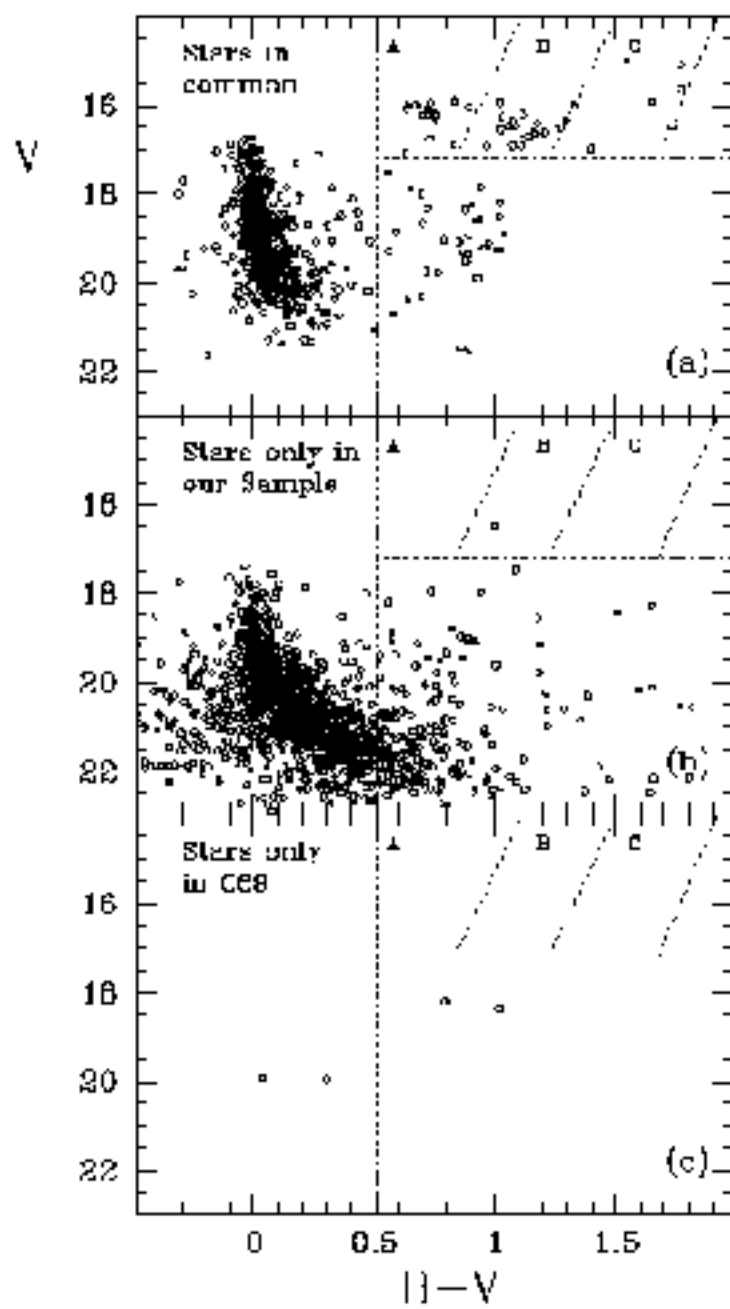


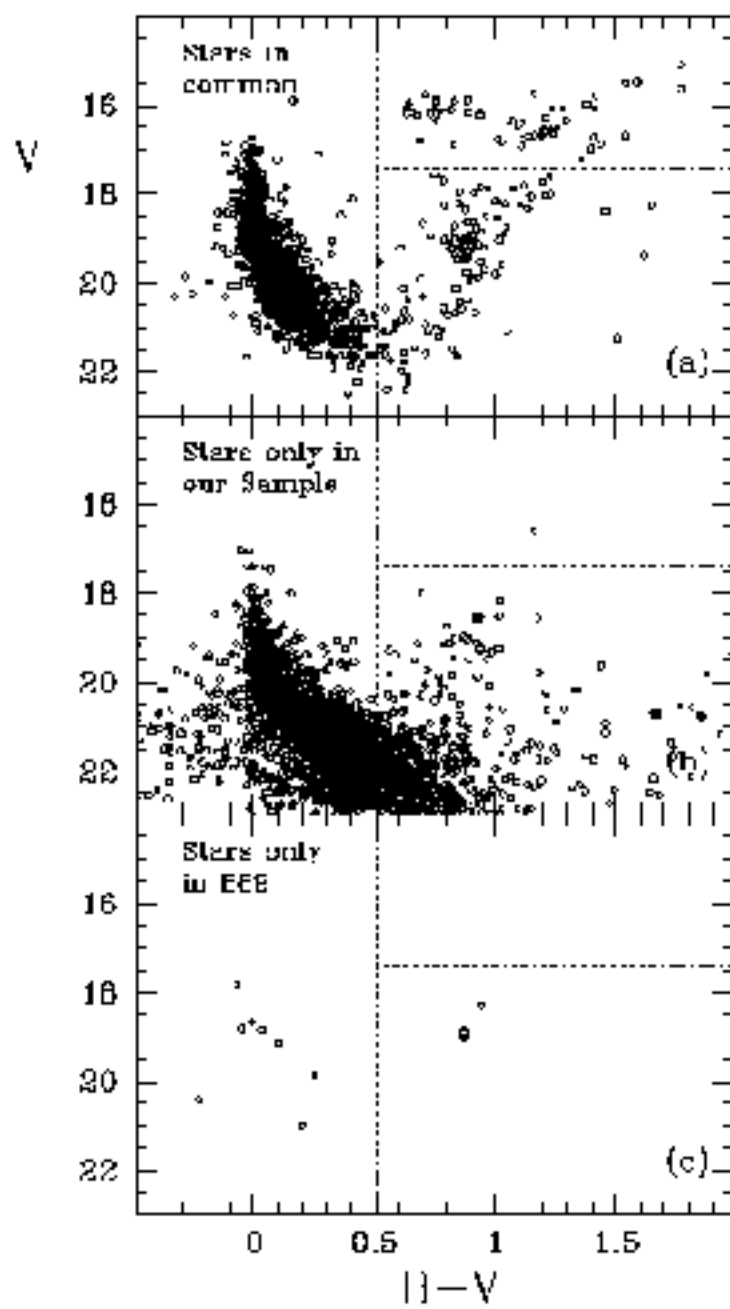












V

